PHYSICS

Chiral flat-band optical cavity with atomically thin mirrors

Daniel G. Suárez-Forero[1]†, Ruihao Ni[2]†, Supratik Sarkar[1]†, Mahmoud Jalali Mehrabad[1]†, Erik Mechtel[1], Valery Simonyan[1], Andrey Grankin[1], Kenji Watanabe[3], Takashi Taniguchi[4], Suji Park[5], Houk Jang[5], Mohammad Hafezi[1]*, You Zhou[2,6]*

A fundamental requirement for photonic technologies is the ability to control the confinement and propagation of light. Widely used platforms include two-dimensional (2D) optical microcavities in which electromagnetic waves are confined in either metallic or distributed Bragg reflectors. Recently, transition metal dichalcogenides hosting tightly bound excitons with high optical quality have emerged as promising atomically thin mirrors. In this work, we propose and experimentally demonstrate a subwavelength 2D nanocavity using two atomically thin mirrors with degenerate resonances. Angle-resolved measurements show a flat band, which sets this system apart from conventional photonic cavities. We demonstrate how the excitonic nature of the mirrors enables the formation of chiral and tunable optical modes upon the application of an external magnetic field. Moreover, we show the electrical tunability of the confined mode. Our work demonstrates a mechanism for confining light with high-quality excitonic materials, opening perspectives for spin-photon interfaces, and chiral cavity electrodynamics.

INTRODUCTION

The ability to confine light to small volumes is central for engineering light-matter interaction in photonic and optoelectronic technologies (*1*–*4*). Planar microcavities are a key platform for confining the spatial extent of electromagnetic waves and manipulating the photonic density of states (*5*, *6*), which has enabled many applications such as filtering (*7*), lasing (*8*), optical detection (*9*), and all-optical switching (*10*, *11*). In these cavities, standing optical modes form between two mirrors, which are traditionally metallic or dielectric (*12*).

In addition to compactness and efficiency, another highly desirable feature for optical devices is chirality (*13*), a characteristic that emerges due to symmetry breaking. Recent research has focused on chiral coupling between light and emitters for classical and quantum optical applications, such as nonreciprocal optical routers and spin-photon interfaces. Examples include engineering polarization-selective spin-photon interfaces in photonic waveguides (*14*–*16*) and ring resonators (*16*–*19*), polaritonic chiral microcavities through magnetic (*20*, *21*) or optical (*22*) manipulation of an active medium hosted in the cavity, and realizing topological photonic states by time-reversal symmetry breaking (*23*). The search for devices with nonreciprocal circular dichroism for different applications extends to other frequency domains such as infrared (*24*) and terahertz (*25*).

Recently, transition metal dichalcogenides (TMDs) have emerged as a new material platform for exploring photon confinement and chiral light-matter coupling. In particular, strong and narrowband reflection has been demonstrated in monolayer $MoSe_2$ thanks to their high optical quality, i.e., a large ratio of radiative (Γ_r) to nonradiative (Γ_{nr}) decay rates (*26*, *27*). The integration of TMDs with photonic structures has also enabled several chiral phenomena—including spin-polarized excitons (*28*), hybrid exciton polaritons (*29*, *30*), and phonon polaritons (*31*)—by leveraging their valley-dependent optical selection rules. In these demonstrations, however, the TMDs are used as the active optical component instead of constituting the photonic structures (*32*, *33*).

In this work, we propose and experimentally demonstrate a method for realizing nanometer-thick planar optical cavities with intrinsic chiral characteristics using two atomically thin TMD mirrors as the fundamental photonic components. In contrast to conventional Fabry-Pérot interferometric cavities, the electromagnetic mode in our system arises via the efficient optical excitation and recombination of excitons in the two TMD mirrors (Fig. 1A). The excitonic nature of the cavity's mirrors endows the system with two desirable features not present in conventional cavities: (i) a momentum-independent optical mode's energy and (ii) spin-polarized cavity modes that split due to the valley Zeeman effect under an external magnetic field. Moreover, we demonstrate the excitonic saturation of the optical mode as a function of pump power and show its tunability via electrical manipulation of each monolayer mirror.

RESULTS

Device design and simulation

The realization of this cavity based on atomically thin materials relies on the high reflection from monolayer $MoSe_2$ at the excitonic resonance. In particular, an optically thin material can act as a narrow-band resonant mirror near its optical resonance. For excitons in atomically thin materials, the reflectance reaches its peak at the exciton wavelength, with a value determined by the ratio Γ_r / Γ_{nr} (see Supplementary Text). Exciton reflectances of more than 85% have been experimentally realized in $MoSe_2$, thanks to the substantial oscillator strengths and relatively low nonradiative rates of the excitons in TMDs when they are encapsulated inside hexagonal boron nitride (hBN) (Fig. 1A) (*26*, *34*). Using such an effect, we can

[1]Joint Quantum Institute (JQI), University of Maryland, College Park, MD 20742, USA. [2]Department of Materials Science and Engineering, University of Maryland, College Park, MD 20742, USA. [3]Research Center for Electronic and Optical Materials, National Institute for Materials Science, 1-1 Namiki, Tsukuba 305-0044, Japan. [4]Research Center for Materials Nanoarchitectonics, National Institute for Materials Science, 1-1 Namiki, Tsukuba 305-0044, Japan. [5]Center for Functional Nanomaterials, Brookhaven National Laboratory, Upton, NY 11973, USA. [6]Maryland Quantum Materials Center, College Park, MD 20742, USA.
*Corresponding author. Email: hafezi@umd.edu (M.H.); youzhou@umd.edu (Y.Z.)
†These authors contributed equally to this work.

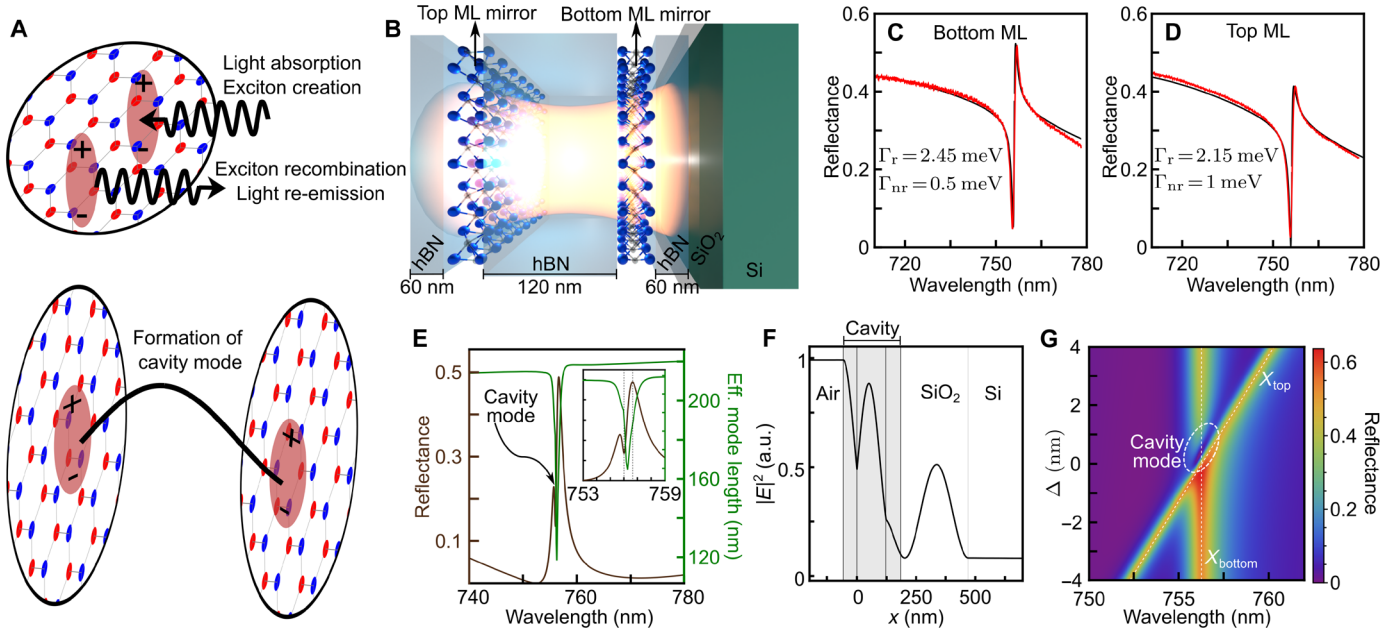

Fig. 1. Design and fabrication of a cavity based on atomically thin mirrors. (**A**) Mechanism for the realization of a nanocavity based on atomically thin mirrors. Top: Because the high optical quality of the exciton in the material, the monolayer (ML) effectively acts as a mirror at the resonant wavelength. Bottom: Stacking two mirrors separated by dielectric material can lead to the formation of optical modes in the structure. (**B**) Schematic representation of the TMD nanocavity device: Two atomically thin $MoSe_2$ mirrors embedded in hBN confine the electromagnetic mode. (**C** and **D**) Individual reflectance spectra of the component monolayers before stacking the final device (red). The black lines show TMM fittings calculated by using a Lorentz oscillator model with the decay rates indicated in each panel. (**E**) Simulation of the device reflectance calculated via TMM simulations. The inset shows a zoom-in of the reflectance and the corresponding mode effective length calculated via FDTD in a reduced range of wavelengths. (**F**) Electric field intensity distribution from FDTD simulation. The minimum in both the reflectance spectrum and effective mode length [(E)] and enhancement of the electric field intensity profile at resonance [(F)] indicate the formation of a standing optical mode. (**G**) TMM simulation of the device's spectrum upon variable exciton energy of the top monolayer X_{top}. X_{bottom} denotes the excitonic resonance of the bottom monolayer and Δ is the detuning between the two layers, $\Delta = X_{top} - X_{bottom}$. The formation of a cavity mode manifests as a minimum in the reflectance for the range of parameters indicated by the dashed white ellipse, and its energy can be manipulated by detuning the resonances of the component $MoSe_2$ mirrors. a.u., arbitrary units.

stack two monolayers vertically to form an optical cavity at the exciton wavelength with a thickness determined by the dielectric spacer (Fig. 1, A and B).

The demonstration of such a cavity, however, imposes substantial experimental challenges. Strains and disorders introduced during the assembly of van der Waals (vdW) heterostructures can not only enhance the nonradiative processes, which reduces the reflectance of the monolayer, but also lead to inhomogeneous broadening and the variation of exciton energies across the samples. This makes it difficult to realize high reflectivity in both TMD monolayers while exactly matching the energies of the reflection peaks. To overcome this challenge, we first assemble a series of hBN-encapsulated monolayer $MoSe_2$ on a silicon substrate and characterize their optical response at 4 K. In doing so, we can select regions of two TMD samples with not only high exciton reflectivity but also similar exciton energy. We then transfer one heterostructure on top of the other to form the cavity. This offers a more controllable way of fabricating cavities as it involves only a single transfer step that will likely introduce less strain and disorders than the full assembly of the vdW structure.

In our experiments, we design the device such that two monolayer mirrors of $MoSe_2$ are embedded inside layers of hBN encapsulation, with a total hBN thickness of 240 nm (Fig. 1B). The monolayers are positioned symmetrically at 60 nm from the top and bottom of the vdW heterostructure and are individually contacted using the Si substrate as a back gate. This gives control over the exciton energies and decay rates (a schematic of the device is shown in Fig. 1B). The thickness of various layers is chosen based on a transfer matrix method (TMM) simulation. We note that the TMDs separation is slightly shorter than half the wavelength of the exciton resonance (in the hBN medium). At precisely the half-wavelength condition, the standing cavity mode becomes optically dark because of the vanishing electric field at the locations of the TMDs and can only decay by nonradiative means. This would be analogous to a Fabry-Pérot cavity with finite absorption loss and zero transmission mirrors (see Supplementary Text for additional discussion). Meanwhile, the total thickness of the hBN obeys the requirement of having minimum reflectance from the SiO_2 substrate-hBN system at the exciton resonance, which facilitates the identification of the optical mode (see Supplementary Text for a complete discussion about the role of the hBN thickness).

Figure 1 (C and D) show the reflectance spectra of two $MoSe_2$ monolayers at 4 K, before they were stacked together to form the cavity. The reflectance spectra can be fitted using the TMM and modeling the 2D material's optical response as a Lorentz oscillator (*26*, *27*, *35*, *36*), from which we extract Γ_r and Γ_{nr} (see Supplementary Text). With this information, we proceed to verify the device design using TMM and finite-difference time-domain (FDTD) simulations and extract reflectance and effective mode length (Fig. 1E and see Materials and Methods for further details). The effective mode length, displayed in the inset, is a measure of the distribution of the optical field, which is equal to the physical thickness of the device for nonresonant wavelengths,

and becomes reduced if there is a localization of the electromagnetic field (see Supplementary Text for its mathematical definition and related discussion). The emergence of a minimum in both the reflectance and effective mode length (Fig. 1E) as well as the electric field intensity distribution (Fig. 1F) confirm the formation of a standing optical mode at a wavelength $\lambda \approx 756$ nm. The enhancement of the electric field inside the cavity volume strongly depends on the substrate, as discussed in the Supplementary Text. FDTD simulations indicate that this optical mode has a quality factor of $Q \approx 1060$ at the resonance wavelength. In the absence of nonradiative losses, the separation between TMDs can be arbitrarily close to $\lambda/2$, with a cavity mode of an infinitely long lifetime. However, nonradiative processes lead to the disappearance of these modes. Therefore, Γ_{nr} sets the limit for how close to $\lambda/2$ the cavity length can be while still having a detectable cavity mode (Supplementary Text).

Figure 1G shows TMM simulations of the reflectance spectrum of such a vdW heterostructure for variable energy detuning between the top (X_{top}) and bottom (X_{bottom}) monolayers' excitons using the obtained values of Γ_r and Γ_{nr} for each monolayer. For detuned resonances, the spectrum shows two individual reflectance peaks, but as one approaches degeneracy, the optical mode establishes, as highlighted by the encircled area in the figure. The simulation predicts a tunability of the cavity mode by changing the detuning between the component mirrors.

Nanocavity device characterization

A microscope picture of the final device is presented in Fig. 2A. The edges of the hBN, top, and bottom $MoSe_2$ monolayers are indicated in black, blue, and red, respectively. The experimental reflectance is presented in Fig. 2B. The narrow dip in the reflectance, in agreement with the prediction in Fig. 1E, confirms the presence of the confined electromagnetic mode in the nanocavity. Figure 2C shows the photoluminescence (PL) spectrum of the sample at the same spot. Unlike reflectance spectra with complex lineshape, the exciton emission (X_0) is a Lorentzian peak centered at the cavity mode. In addition, a secondary peak from charged excitonic states ($X^{\pm}$) is detected at longer wavelengths, which is not resonant with the optical mode (*37*). A particular feature of this architecture is shown in Fig. 2 (D and E): The cavity mode presents a flat momentum dispersion. This is verified both theoretically via TMM simulations (Fig. 2D) and experimentally by realizing Fourier spectroscopic measurements of the far-field of the cavity mode (Fig. 2E). In conventional planar cavities, varying angles lead to different optical path lengths and phases. In our design, the exciton energy is agnostic to varying angles of incidence, and the propagation phase is canceled out by the wavelength-dependent phase of the Lorentz oscillator, making the cavity dispersion flat. Further discussion about the origin of this flat band can be found in Supplementary Text.

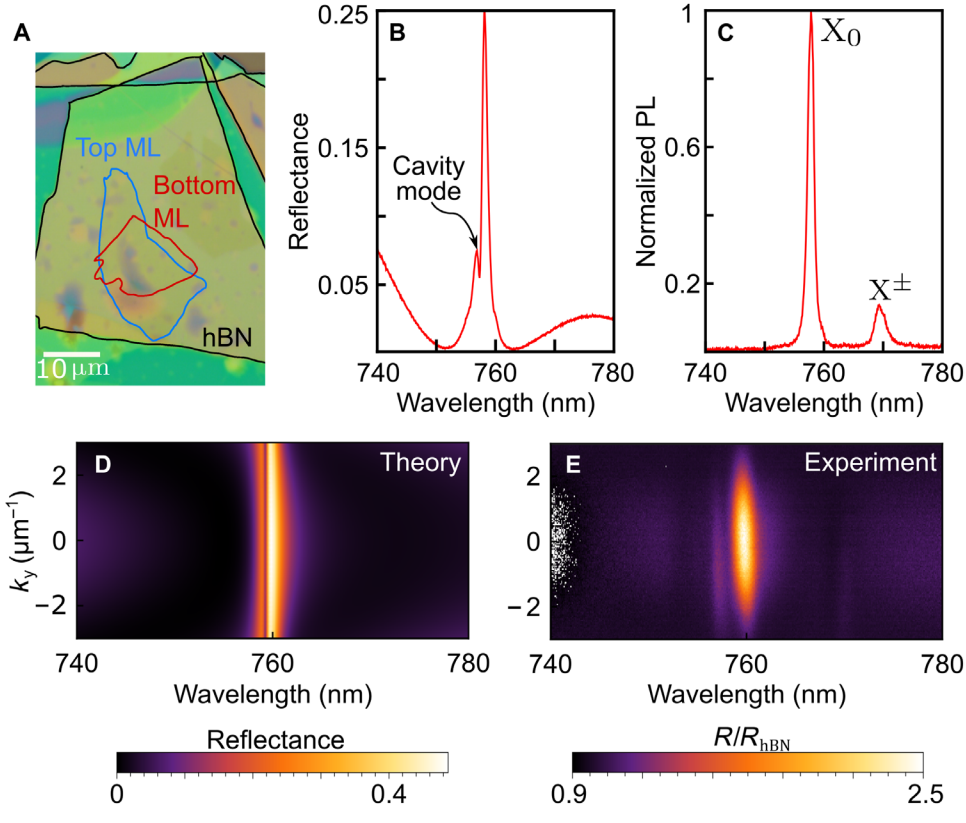

Fig. 2. Experimental characterization of the cavity sample. (**A**) Microscope picture of the nano-cavity device with hBN layers and $MoSe_2$ bottom and top layers indicated in black, red, and blue, respectively. (**B**) Experimental reflectance spectrum of the device. As theoretically predicted, the confined optical mode manifests as a narrow minimum in the reflectance spectrum (indicated by the arrow). (**C**) PL spectrum of the device. The central emission (X_0) coincides with the device's resonant wavelength. A secondary peak from charged excitonic states is observed at longer wavelengths ($X^{\pm}$). (**D**) Nanocavity dispersion calculated via TMM simulation. The confinement mechanism makes the cavity mode flat within our numerical aperture. (**E**) Experimental dispersion of the device measured via far-field imaging. As theoretically predicted, the optical mode is flat in momentum.

Magnetically induced chirality

The excitonic origin of the high reflectance in the monolayer TMD mirrors endows the nanocavity with another unique capability, i.e., a chiral behavior induced by an external magnetic field (**B**). A potential application of such a chiral cavity is the circular polarization-dependent light-matter interaction that can be achieved when embedding an unpolarized emitter resonant with one of the chiral modes. In this scenario, the emitter will be transparent to one of the cavity modes, but interact with the other one (*38*). To demonstrate this chirality, we measure the **B**-dependent reflectance when illuminating the sample with opposite circular polarization (σ^+ and σ^-) in a Faraday configuration (see Materials and Methods). Figure 3A shows the reflectance spectra of the device for the two circular polarization states under three different values of **B**: 0, 5, and 10 T. We note that this measurement was performed in a different spot on the sample with respect to Fig. 2, resulting in slight spectral differences. The small difference between the σ^+ and σ^- spectra at 0 T originates in the imperfect polarization filter. Regardless, the degeneracy of the mode is evident in the absence of a magnetic field. This degeneracy of the two optical modes with orthogonal circular polarization is lifted with increasing **B**. This behavior originates in the valley-dependent optical selection rule and the valley Zeeman effect of TMD monolayers due to inversion symmetry breaking and spin-orbit coupling (*39*, *40*): A magnetic field splits the energy of excitons in the K and $-K$ valleys, which shift the reflectance peak and the cavity mode of σ^+ and σ^- light (inset of Fig. 3A). This magnetic tuning of chiral light-matter coupling is usually not achievable in photonic microcavities due to the nonmagnetic nature of the typical component materials (*6*). Here, excitons in $MoSe_2$ experience the Zeeman effect, which introduces the chiral behavior.

To perform a quantitative analysis of the cavity's chiral behavior, we collect data over the range of 0 to 10 T. The reflective circular dichroism (RCD), defined as $\frac{R^+ - R^-}{R^+ + R^-}$, where $R^{+(-)}$ is the reflectance of the polarization $\sigma^{+(-)}$, is shown in Fig. 3B. The chiral behavior manifests as an increasing RCD with increasing magnetic field **B**, which reaches a value of 0.41 at the highest magnetic field of 10 T. By fitting the energy splitting of the two chiral modes in response to the magnetic field to the relationship $\Delta E = g\mu_B B$ (where μ_B is the Bohr magneton), we obtain $g = -4.46 \pm 0.45$. The extracted g factor is in good agreement with previously reported values and theoretical predictions (*32*, *41*, *42*). Measurements of the magnetically induced chirality performed on a third spot of the sample show consistent results (Supplementary Text).

Electrical tuning and thermal response of the optical mode

We now demonstrate some of the mechanisms that can be implemented to obtain control over the optical mode. In Fig. 4, we show that the resonance can be modified by electrical gating and optical pumping. Each monolayer mirror is individually electrically contacted as detailed in Materials and Methods. As shown in Fig. 4A as a proof of principle, the electrical gating allows us to turn on and off the mode in real time and to tune its energy (Fig. 4B shows an inset

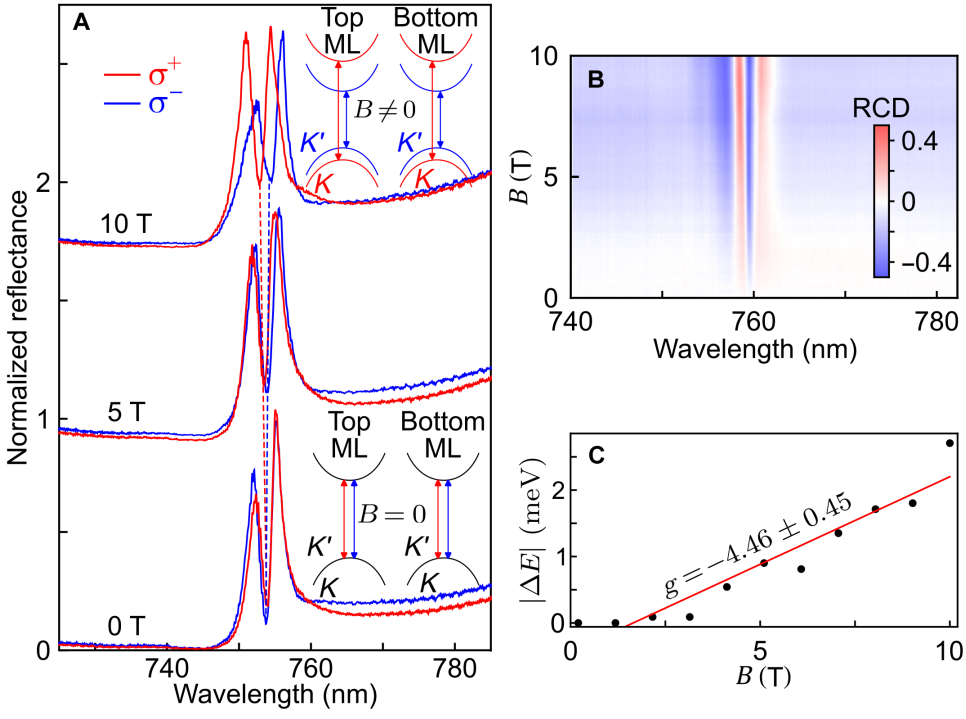

Fig. 3. Chiral behavior induced by an external magnetic field *B*. (**A**) Device's reflectance spectra for the orthogonal circular polarization states σ^+ (red) and σ^- (blue) at three different values of **B**: 0 T (bottom), 5 T (middle), and 10 T (top). The insets show a depiction of the mechanism by which the chirality is established: The modes are degenerate in the absence of a magnetic field (black scheme), but the mode splits in the presence of a magnetic field and exhibits a chiral light-matter response (red and blue scheme). The data are collected at a different spot than Fig. 2. (**B**) Reflective circular dichroism (RCD) of the nanocavity device for increasing **B**. (**C**) Energy difference between the σ^+ and σ^- cavity modes as a function of **B**. A linear regression indicates a value of the magnetic factor $g = -4.46 \pm 0.45$, in good agreement with reported values and theoretical predictions.

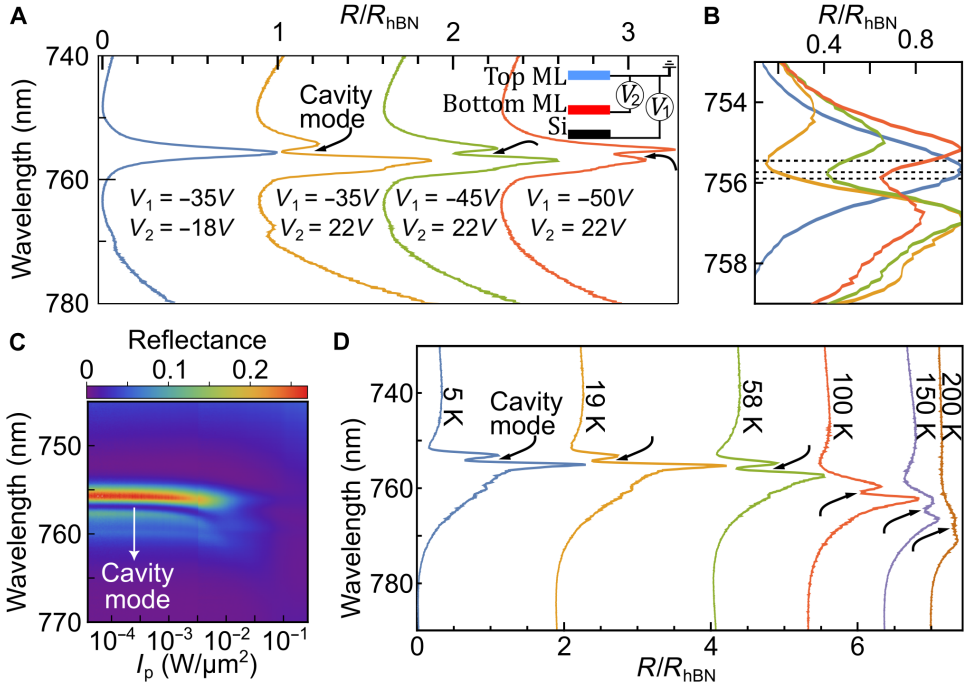

Fig. 4. Tuning mechanisms of the optical mode. (**A**) Independent electrical contacts on each $MoSe_2$ mirror (as shown in the inset) give control over the charge density and hence over the excitonic resonance energy and oscillator strength. As a result, the cavity mode can be turned off (blue line), or it can be tuned over a range of ~0.5 nm, as shown in (**B**). (**C**) Pump intensity–dependent reflectance spectrum. The pump intensity axis (horizontal) does not follow a linear trend, because the power was not modified linearly. As the pump power increases, the optical mode red-shifts and broadens due to thermal fluctuations and saturation of the TMDs. After a critical intensity $I_p \approx 7 \times 10^{-3}$ W/ μm², the mode completely vanishes. (**D**) Temperature dependence of the optical mode collected with a 10^{-4} W/μm² white pump. The data show a tunability of ≈ 10 nm in the range of 4 to 100 K. At $T = 200$ K the mode is not identifiable anymore. In (A) and (D), the arrows serve as a guide for the eye to track the modification of the optical mode.

of the resonance with continuous tunability of ~0.5 nm). Further optimization of the gates can lead to greater tunability at lower voltages. The optical power also offers a control tool over the cavity resonance. Figure 4C shows the reflectance spectra of the sample when excited by a supercontinuum white laser (with a pulse duration of ≈1 ns) at varying power levels. The cavity mode is not notably modified below $I_p \approx 10^{-3}$ W/ μm². Upon further increasing the laser intensity, the mode red-shifts and broadens. Last, above a threshold pump intensity $I_p \approx 7 \times 10^{-3}$ W/ μm², the excitonic response and the cavity mode disappear in the reflectance spectra. This response to increasing pump powers could stem from the subsequent saturation of the exciton resonance and the laser-induced exciton decoherence (linewidth broadening and increasing Γ_{nr}).

We therefore further investigate the thermal effects by measuring the reflectance spectra at different temperatures, as shown in Fig. 4D. We normalize the device's reflectance to that of a region without TMDs but with the same hBN thickness at each temperature. With increasing temperatures, the exciton and optical modes broaden and red-shift, in a similar fashion observed in Fig. 4C. The optical mode is robust up to a temperature $T \approx 100$ K, while the temperature tunes cavity mode over a range of ≈ 10 nm with a mode broadening of a factor ≈ 1.3. The thermal fluctuations enhance the nonradiative decay rate of the exciton by promoting the exciton-phonon decoherence, reducing the ratio Γ_r / Γ_{nr} to the critical point where the mode vanishes at $T \approx 200$ K (*43*, *44*).

DISCUSSION

We demonstrate a mechanism to achieve light confinement by harnessing the high quality of the optical excitations in TMD materials, using them as atomically thin mirrors. The 2D nature of the constituent mirrors endows this device with advantages in terms of miniaturization and integration capabilities with a *Q* factor comparable to traditionally used planar cavities (see table S1). Future improvements in the materials' quality and heterostructure fabrication, such as nano-squeegee (*45*) and laser annealing (*46*, *47*), could further reduce their optical loss by decreasing the nonradiative and inhomogeneous broadening associated with disorders and lead to large-area samples. For instance, TMD monolayers grown by chemical vapor deposition have been shown to exhibit optical quality comparable with the best hBN-encapsulated samples (*46*, *47*).

The demonstrated flat dispersion sets this architecture apart from conventional planar cavities, which have a strong angular dependence on the resonant mode energy. The weak dispersion of a TMD cavity can enable the efficient control of point emitters, for example, quantum emitters in 2D materials (*48*–*51*), without complicated photonic structures such as photonic crystals and curved mirrors. Furthermore, such a concept can be extended to other resonant optical effects in not only 2D materials [including other TMDs and hBN (*52*)] but also other optically thin systems, which could enable a wide range of optical applications covering visible and infrared spectra.

The unique properties of chiral cavities have been proposed for the realization of nonequilibrium states of matter and new topological effects (*53*–*55*). Other architectures have been demonstrated to host chiral optical modes (*56*), and our design opens an alternative to exploring these configurations in a vdW heterostructure. There are also intriguing analogies between a TMD mirror and a dipole array of cold atoms (*57*) that could make this architecture suitable for the study of subradiant/superradiant states and other collective effects in a condensed matter setting (*58*). The demonstrated electrical tuning of the cavity resonance enables a dynamic control for devices such as tunable optical isolators and polarization-dependent light-microwave transductors (*59*, *60*). Furthermore, optically pumping of the valley polarization in TMDs opens up the intriguing possibility of ultrafast optical control of the chiral light-matter coupling (*29*, *61*–*64*). Last, motivated by recent observations of strongly interacting excitons in hetero-bilayer TMDs superlattice structures (*65*–*67*), one can envisage embedding these lattices inside our planar cavity and explore the rich physics of Bose-Hubbard polaritonic models (*68*, *69*).

MATERIALS AND METHODS

TMM and FDTD numerical simulations

For the numerical simulations of the device's reflectance, we apply the TMM by using the refractive indices of the different materials from a database. In this formalism, we simulate the response of the system to an incoming plane wave at any angle, which in this case was chosen to be 0° (except for Fig. 2C, where we calculate the angular dependence). For the calculation of the electric field intensity profile, effective cavity mode length, and Q factor, we rely on a FDTD simulation implemented in commercial software. We simulate the situations of the cavity excited through an embedded dipole source or by an incident plane wave.

Device fabrication

Monolayer $MoSe_2$ and hBN flakes are exfoliated from bulk crystals on top of silicon substrates with an oxide layer of 285 nm. High optical quality monolayers of $MoSe_2$ are obtained using the QPress Exfoliator at Center for Functional Nanomaterials in Brookhaven National Laboratory. The $MoSe_2$ flakes are identified under an optical microscope and confirmed by PL measurements. The thickness of hBN flakes is verified by atomic force microscopy. The device is assembled by the vdW dry transfer technique. We first fabricate several hBN/$MoSe_2$/hBN heterostructures and characterize them by PL and reflectance measurements to find the ideal spot. Last, to obtain the nanocavity device, two heterostructures with identical excitonic energies and high radiative decay rates are carefully chosen and stacked together.

Fabrication of electrical contacts

To expose and contact the $MoSe_2$ monolayers respectively, we first define the area of etching using electron-beam lithography and etch the hBN using inductively coupled plasma reactive ion etcher. Then, we make the electrical contacts to both $MoSe_2$ monolayers using chromium (5 nm) and gold (90 nm) deposited via thermal evaporation to connect them to the wire-bonding pads.

Setup for optical measurements

The sample is held at a temperature of 6 K in a closed-loop cryostat. For the optical measurements, we use a confocal microscopy setup in a reflectance configuration. The focused laser spot on the sample is about 1 μm in diameter. A tungsten lamp and a supercontinuum white laser are used as broadband light sources; there is no difference in the results obtained with each source. For PL measurements, we use a HeNe laser (≈ 633 nm) to excite the material. For the measurements of the magnetic field dependence, polarization-resolved reflectance spectra were collected by placing a quarter-wave plate followed by a linear polarizer in the detection path. The signal is lastly collected by a charge-coupled device attached to a spectrometer. A detailed description of this setup can be found in (*70*).

Supplementary Materials

This PDF file includes:

Supplementary Text
Figs. S1 to S11
Table S1
References

REFERENCES AND NOTES

1. J. L. O'Brien, A. Furusawa, J. Vučković, Photonic quantum technologies. *Nat. Photonics* **3**, 687–695 (2009).
2. I. Carusotto, C. Ciuti, Quantum fluids of light. *Rev. Mod. Phys.* **85**, 299–366 (2013).
3. D. E. Chang, V. Vuletić, M. D. Lukin, Quantum nonlinear optics–photon by photon. *Nat. Photonics* **8**, 685–694 (2014).
4. J. Bloch, A. Cavalleri, V. Galitski, M. Hafezi, A. Rubio, Strongly correlated electron–photon systems. *Nature* **606**, 41–48 (2022).
5. K. J. Vahala, Optical microcavities. *Nature* **424**, 839–846 (2003).
6. H. Megahd, D. Comoretto, P. Lova, (INVITED)Planar microcavities: Materials and processing for light control. *Opt. Mater.: X* **13**, 100130 (2022).
7. F. Monifi, Ş. K. Özdemir, L. Yang, Tunable add-drop filter using an active whispering gallery mode microcavity. *Appl. Phys. Lett.* **103**, 181103 (2013).
8. R. Michalzik, VCSEL fundamentals. *Springer Ser. Opt. Sci.* **166**, 19–75 (2013).
9. M. Furchi, A. Urich, A. Pospischil, G. Lilley, K. Unterrainer, H. Detz, P. Klang, A. M. Andrews, W. Schrenk, G. Strasser, T. Mueller, Microcavity-integrated graphene photodetector. *Nano Lett.* **12**, 2773–2777 (2012).
10. G. Ma, J. Shen, Z. Zhang, Z. Hua, S. H. Tang, Ultrafast all-optical switching in one-dimensional photonic crystal with two defects. *Opt. Express* **14**, 858–865 (2006).
11. H. Nakamura, Y. Sugimoto, K. Kanamoto, N. Ikeda, Y. Tanaka, Y. Nakamura, S. Ohkouchi, Y. Watanabe, K. Inoue, H. Ishikawa, K. Asakawa, Ultra-fast photonic crystal/quantum dot alloptical switch for future photonic networks. *Opt. Express* **12**, 6606–6614 (2004).
12. A. Kavokin, J. J. Baumberg, G. Malpuech, F. P. Laussy, *Microcavities* (Oxford Science, ed. 2, 2007).
13. P. Lodahl, S. Mahmoodian, S. Stobbe, A. Rauschenbeutel, P. Schneeweiss, J. Volz, H. Pichler, P. Zoller, Chiral quantum optics. *Nature* **541**, 473–480 (2017).
14. I. Söllner, S. Mahmoodian, S. L. Hansen, L. Midolo, A. Javadi, G. Kiršanskė, T. Pregnolato, H. El-Ella, E. H. Lee, J. D. Song, S. Stobbe, P. Lodahl, Deterministic photon-emitter coupling in chiral photonic circuits. *Nat. Nanotechnol.* **10**, 775–778 (2015).
15. S. Barik, A. Karasahin, C. Flower, T. Cai, H. Miyake, W. DeGottardi, M. Hafezi, E. Waks, A topological quantum optics interface. *Science* **359**, 666–668 (2018).
16. M. J. Mehrabad, S. Mittal, M. Hafezi, Topological photonics: Fundamental concepts, recent developments, and future directions. *Phys. Rev. A* **108**, 040101 (2023).
17. S. Barik, A. Karasahin, S. Mittal, E. Waks, M. Hafezi, Chiral quantum optics using a topological resonator. *Phys. Rev. B* **101**, 205303 (2020).
18. M. Jalali Mehrabad, A. Foster, R. Dost, E. Clarke, P. Patil, I. Farrer, J. Heffernan, M. Skolnick, L. Wilson, A semiconductor topological photonic ring resonator. *Appl. Phys. Lett.* **116**, 061102 (2020).
19. M. J. Mehrabad, A. P. Foster, R. Dost, E. Clarke, P. K. Patil, A. M. Fox, M. S. Skolnick, L. R. Wilson, Chiral topological photonics with an embedded quantum emitter. *Optica* **7**, 1690–1696 (2020).
20. T. P. Lyons, D. J. Gillard, C. Leblanc, J. Puebla, D. D. Solnyshkov, L. Klompmaker, I. A. Akimov, C. Louca, P. Muduli, A. Genco, M. Bayer, Y. Otani, G. Malpuech, A. I. Tartakovskii, Giant effective Zeeman splitting in a monolayer semiconductor realized by spin-selective strong light-matter coupling. *Nat. Photonics* **16**, 632–636 (2022).
21. D. G. Suárez-Forero, D. W. Session, M. Jalali Mehrabad, P. Knüppel, S. Faelt, W. Wegscheider, M. Hafezi, Spin-selective strong light-matter coupling in a 2D hole gas-microcavity system. *Nat. Photonics* **17**, 1–5 (2023).
22. N. Carlon Zambon, P. St-Jean, M. Milićević, A. Lemaître, A. Harouri, L. Le Gratiet, O. Bleu, D. Solnyshkov, G. Malpuech, I. Sagnes, S. Ravets, A. Amo, J. Bloch, Optically controlling the emission chirality of microlasers. *Nat. Photonics* **13**, 283–288 (2019).

23. S. Klembt, T. Harder, O. Egorov, K. Winkler, R. Ge, M. Bandres, M. Emmerling, L. Worschech, T. Liew, M. Segev, C. Schneider, S. Höfling, Exciton-polariton topological insulator. *Nature* **562**, 552–556 (2018).
24. Q. Du, C. Wang, Y. Zhang, Y. Zhang, T. Fakhrul, W. Zhang, C. Gonçalves, C. Blanco, K. Richardson, L. Deng, Monolithic on-chip magneto-optical isolator with 3 dB insertion loss and 40 dB isolation ratio. *ACS Photonics* **5**, 5010–5016 (2018).
25. Q. Mu, F. Fan, S. Chen, S. Xu, C. Xiong, X. Zhang, X. Wang, S. Chang, Tunable magneto-optical polarization device for terahertz waves based on InSb and its plasmonic structure. *Photonics Res.* **7**, 325–331 (2019).
26. G. Scuri, Y. Zhou, A. A. High, D. S. Wild, C. Shu, K. D. Greve, L. A. Jauregui, T. Taniguchi, K. Watanabe, P. Kim, M. D. Lukin, H. Park, Large excitonic reflectivity of monolayer $MoSe_2$ encapsulated in hexagonal boron nitride. *Phys. Rev. Lett.* **120**, 037402 (2018).
27. P. Back, S. Zeytinoglu, A. Ijaz, M. Kroner, A. Imamoğlu, Realization of an electrically tunable narrow-bandwidth atomically thin mirror using monolayer $MoSe_2$. *Phys. Rev. Lett.* **120**, 037401 (2018).
28. R. Shreiner, K. Hao, A. Butcher, A. A. High, Electrically controllable chirality in a nanophotonic interface with a two-dimensional semiconductor. *Nat. Photonics* **16**, 330–336 (2022).
29. W. Liu, Z. Ji, Y. Wang, G. Modi, M. Hwang, B. Zheng, V. J. Sorger, A. Pan, R. Agarwal, Generation of helical topological exciton-polaritons. *Science* **370**, 600–604 (2020).
30. M. Li, I. Sinev, F. Benimetskiy, T. Ivanova, E. Khestanova, S. Kiriushechkina, A. Vakulenko, S. Guddala, M. Skolnick, V. M. Menon, , D. Krizhanovskii, A. Alù, A. Samusev, A. B. Khanikaev, Experimental observation of topological Z2 exciton-polaritons in transition metal dichalcogenide monolayers. *Nat. Commun.* **12**, 4425 (2021).
31. S. Guddala, F. Komissarenko, S. Kiriushechkina, A. Vakulenko, M. Li, V. Menon, A. Alù, A. Khanikaev, Topological phonon-polariton funneling in midinfrared metasurfaces. *Science* **374**, 225–227 (2021).
32. A. Srivastava, M. Sidler, A. V. Allain, D. S. Lembke, A. Kis, A. Imamoglu, Valley Zeeman effect in elementary optical excitations of monolayer WSe_2. *Nat. Phys.* **11**, 141–147 (2015).
33. X. Xu, W. Yao, D. Xiao, T. F. Heinz, Spin and pseudospins in layered transition metal dichalcogenides. *Nat. Phys.* **10**, 343–350 (2014).
34. F. Cadiz, E. Courtade, C. Robert, G. Wang, Y. Shen, H. Cai, T. Taniguchi, K. Watanabe, H. Carrere, D. Lagarde, M. Manca, T. Amand, P. Renucci, S. Tongay, X. Marie, B. Urbaszek, Excitonic linewidth approaching the homogeneous limit in MoS_2-based van der Waals heterostructures. *Phys. Rev. X* **7**, 021026 (2017).
35. P. Y. Yu, M. Cardona, *Fundamentals of Semiconductors* (Springer, ed. 4, 2010).
36. M. M. Glazov, T. Amand, X. Marie, D. Lagarde, L. Bouet, B. Urbaszek, Exciton fine structure and spin decoherence in monolayers of transition metal dichalcogenides. *Phys. Rev. B* **89**, 201302 (2014).
37. G. D. Shepard, J. V. Ardelean, O. A. Ajayi, D. Rhodes, X. Zhu, J. C. Hone, S. Strauf, Trion-species-resolved quantum beats in $MoSe_2$. *ACS Nano* **11**, 11550–11558 (2017).
38. D. Hallett, A. P. Foster, D. Whittaker, M. S. Skolnick, L. R. Wilson, Engineering chiral light–matter interactions in a waveguide-coupled nanocavity. *ACS Photonics* **9**, 706–713 (2022).
39. D. Xiao, G. B. Liu, W. Feng, X. Xu, W. Yao, Coupled spin and valley physics in monolayers of MoS_2 and other group-VI dichalcogenides. *Phys. Rev. Lett.* **108**, 196802 (2012).
40. F. Xuan, S. Y. Quek, Valley Zeeman effect and Landau levels in two-dimensional transition metal dichalcogenides. *Phys. Rev. Res.* **2**, 033256 (2020).
41. G. Aivazian, Z. Gong, A. M. Jones, R.-L. Chu, J. Yan, D. G. Mandrus, C. Zhang, D. Cobden, W. Yao, X. Xu, Magnetic control of valley pseudospin in monolayer WSe_2. *Nat. Phys.* **11**, 148–152 (2015).
42. C. Robert, H. Dery, L. Ren, D. Van Tuan, E. Courtade, M. Yang, B. Urbaszek, D. Lagarde, K. Watanabe, T. Taniguchi, T. Amand, X. Marie, Measurement of conduction and valence bands g-factors in a transition metal dichalcogenide monolayer. *Phys. Rev. Lett.* **126**, 067403 (2021).
43. T. Jakubczyk, K. Nogajewski, M. R. Molas, M. Bartos, W. Langbein, M. Potemski, J. Kasprzak, Impact of environment on dynamics of exciton complexes in a WS_2 monolayer. *2D Mater.* **5**, 031007 (2018).
44. I. Epstein, B. Terrés, A. J. Chaves, V.-V. Pusapati, D. A. Rhodes, B. Frank, V. Zimmermann, Y. Qin, K. Watanabe, T. Taniguchi, H. Giessen, S. Tongay, J. C. Hone, N. M. R. Peres, F. H. L. Koppens, Near-unity light absorption in a monolayer WS_2 Van der Waals heterostructure cavity. *Nano Lett.* **20**, 3545–3552 (2020).
45. M. R. Rosenberger, H.-J. Chuang, K. M. McCreary, A. T. Hanbicki, S. V. Sivaram, B. T. Jonker, Nano-"queegee" for the creation of clean 2D material interfaces. *ACS Appl. Mater. Interfaces* **10**, 10379–10387 (2018).
46. S. Shree, A. George, T. Lehnert, C. Neumann, M. Benelajla, C. Robert, X. Marie, K. Watanabe, T. Taniguchi, U. Kaiser, B. Urbaszek, A. Turchanin, High optical quality of MoS_2 monolayers grown by chemical vapor deposition. *2D Mater.* **7**, 015011 (2020).
47. C. Rogers, D. Gray, N. Bogdanowicz, H. Mabuchi, Laser annealing for radiatively broadened $MoSe_2$ grown by chemical vapor deposition. *Phys. Rev. Mater.* **2**, 094003 (2018).
48. C. Palacios-Berraquero, D. M. Kara, A. R.-P. Montblanch, M. Barbone, P. Latawiec, D. Yoon, A. K. Ott, M. Loncar, A. C. Ferrari, M. Atatüre, Large-scale quantum-emitter arrays in atomically thin semiconductors. *Nat. Commun.* **8**, 15093 (2017).
49. S. I. Azzam, K. Parto, G. Moody, Prospects and challenges of quantum emitters in 2D materials. *Appl. Phys. Lett.* **118**, 240502 (2021).
50. D. Thureja, F. E. Yazici, T. Smolenski, M. Kroner, D. J. Norris, A. Imamoglu, Electrically defined quantum dots for bosonic excitons. arXiv:2402.19278 [cond-mat.mes-hall] (2024).
51. A. Srivastava, M. Sidler, A. V. Allain, D. S. Lembke, A. Kis, A. Imamoğlu, Optically active quantum dots in monolayer WSe_2. *Nature Nanotechnol.* **10**, 491–496 (2015).
52. E. Y. Ma, J. Hu, L. Waldecker, K. Watanabe, T. Taniguchi, F. Liu, T. F. Heinz, The Reststrahlen effect in the optically thin limit: A framework for resonant response in thin media. *Nano Lett.* **22**, 8389–8393 (2022).
53. H. Hübener, U. De Giovannini, C. Schäfer, J. Andberger, M. Ruggenthaler, J. Faist, A. Rubio, Engineering quantum materials with chiral optical cavities. *Nat. Mater.* **20**, 438–442 (2020).
54. C. B. Dag, V. Rokaj, Cavity induced topology in graphene. arXiv:2311.02806 [cond-mat.mes-hall] (2023).
55. C. Jiang, M. Baggioli, Q.-D. Jiang, Engineering flat bands in twisted-bilayer graphene away from the magic angle with chiral optical cavities. arXiv:2306.05149 [cond-mat.mes-hall] (2023).
56. K. Rechcińska, M. Król, R. Mazur, P. Morawiak, R. Mirek, K. Łempicka, W. Bardyszewski, M. Matuszewski, P. Kula, W. Piecek, P. G. Lagoudakis, B. Pietka, J. Szczytko, Engineering spin-orbit synthetic Hamiltonians in liquid-crystal optical cavities. *Science* **366**, 727–730 (2019).
57. J. Rui, D. Wei, A. Rubio-Abadal, S. Hollerith, J. Zeiher, D. M. Stamper-Kurn, C. Gross, I. Bloch, A subradiant optical mirror formed by a single structured atomic layer. *Nature* **583**, 369–374 (2020).
58. P. O. Guimond, A. Grankin, D. V. Vasilyev, B. Vermersch, P. Zoller, Subradiant bell states in distant atomic arrays. *Phys. Rev. Lett.* **122**, 093601 (2019).
59. Y. Zhou, G. Scuri, J. Sung, R. Gelly, D. Wild, K. D. Greve, A. Joe, T. Taniguchi, K. Watanabe, P. Kim, M. Lukin, H. Park, Controlling excitons in an atomically thin membrane with a mirror. *Phys. Rev. Lett.* **124**, 027401 (2020).
60. X. Gao, Z.-Q. Yin, T. Li, High-speed quantum transducer with a single-photon emitter in a 2D resonator. *Annalen der Physik* **532**, 2000233 (2020).
61. S. Guddala, Y. Kawaguchi, F. Komissarenko, S. Kiriushechkina, A. Vakulenko, K. Chen, A. Alù, V. M. Menon, A. B. Khanikaev, All-optical nonreciprocity due to valley polarization pumping in transition metal dichalcogenides. *Nat. Commun.* **12**, 3746 (2021).
62. Z. Sun, J. Gu, A. Ghazaryan, Z. Shotan, C. R. Considine, M. Dollar, B. Chakraborty, X. Liu, P. Ghaemi, S. Kéna-Cohen, V. M. Menon, Optical control of room-temperature valley polaritons. *Nat. Photonics* **11**, 491–496 (2017).
63. K. Hao, R. Shreiner, A. Kindseth, A. A. High, Optically controllable magnetism in atomically thin semiconductors. *Sci. Adv.* **8**, eabq7650 (2022).
64. G. Wang, A. Chernikov, M. M. Glazov, T. F. Heinz, X. Marie, T. Amand, B. Urbaszek, *Colloquium*: Excitons in atomically thin transition metal dichalcogenides. *Rev. Mod. Phys.* **90**, 021001 (2018).
65. R. Xiong, J. H. Nie, S. L. Brantly, P. Hays, R. Sailus, K. Watanabe, T. Taniguchi, S. Tongay, C. Jin, Correlated insulator of excitons in WSe_2/WS_2 moiré superlattices. *Science* **380**, 860–864 (2023).
66. H. Park, J. Zhu, X. Wang, Y. Wang, W. Holtzmann, T. Taniguchi, K. Watanabe, J. Yan, L. Fu, T. Cao, D. Xiao, D. R. Gamelin, H. Yu, W. Yao, X. Xu, Dipole ladders with large Hubbard interaction in a moiré exciton lattice. *Nat. Phys.* **19**, 1286–1292 (2023).
67. B. Gao, D. G. Suárez-Forero, S. Sarkar, T.-S. Huang, D. Session, M. J. Mehrabad, R. Ni, M. Xie, P. Upadhyay, J. Vannucci, S. Mittal, K. Watanabe, T. Taniguchi, A. Imamoglu, Y. Zhou, M. Hafezi, Excitonic Mott insulator in a Bose-Fermi-Hubbard system of moiré WS_2/WSe_2 heterobilayer. *Nat. Commun.* **15**, 2305 (2024).
68. D. G. Angelakis, Quantum simulations with photons and polaritons. *Quantum Science and Technology* (Springer, 2017), vol. 134.
69. M. J. Hartmann, Quantum simulation with interacting photons. *J. Optics* **18**, 104005 (2016).
70. J. C. Sell, J. R. Vannucci, D. G. Suárez-Forero, B. Cao, D. W. Session, H.-J. Chuang, K. M. Mccreary, M. R. Rosenberger, B. T. Jonker, S. Mittal, M. Hafezi, Magneto-optical measurements of the negatively charged *2s* exciton in WSe_2. *Phys. Rev. B* **106**, 81409 (2022).
71. E. D. Palik, *Handbook of Optical Constants of Solids* (Elsevier, 1985).
72. T. LaMountain, J. Nelson, E. J. Lenferink, S. H. Amsterdam, A. A. Murthy, H. Zeng, T. J. Marks, V. P. Dravid, M. C. Hersam, N. P. Stern, Valley-selective optical Stark effect of exciton-polaritons in a monolayer semiconductor. *Nat. Commun.* **12**, 4530 (2021).
73. C. Zhao, T. Norden, P. Zhang, P. Zhao, Y. Cheng, F. Sun, J. P. Parry, P. Taheri, J. Wang, Y. Yang, T. Scrace, K. Kang, S. Yang, G.-x. Miao, R. Sabirianov, G. Kioseoglou, W. Huang, A. Petrou, H. Zeng, Enhanced valley splitting in monolayer WSe_2 due to magnetic exchange field. *Nat. Nanotechnol.* **12**, 757–762 (2017).

74. T. Norden, C. Zhao, P. Zhang, R. Sabirianov, A. Petrou, H. Zeng, Giant valley splitting in monolayer WS_2 by magnetic proximity effect. *Nat. Commun.* **10**, 4163 (2019).
75. C. Anton-Solanas, M. Waldherr, M. Klaas, H. Suchomel, T. H. Harder, H. Cai, E. Sedov, S. Klembt, A. V. Kavokin, S. Tongay, K. Watanabe, T. Taniguchi, S. Höfling, C. Schneider, Bosonic condensation of exciton–polaritons in an atomically thin crystal. *Nat. Mater.* **20**, 1233–1239 (2021).
76. K. Peng, W. Li, M. Sun, J. D. Rivero, C. Ti, X. Han, L. Ge, L. Yang, X. Zhang, W. Bao, Topological valley Hall polariton condensation. *Nat. Nanotechnol.* **19**, 1283–1289 (2024).
77. E. Y. Paik, L. Zhang, S. Hou, H. Zhao, Y.-H. Chou, S. R. Forrest, H. Deng, High quality factor microcavity for van der waals semiconductor polaritons using a transferrable mirror. *Adv. Opt. Mater.* **11**, 2201440 (2023).
78. R. Pandya, A. Ashoka, K. Georgiou, J. Sung, R. Jayaprakash, S. Renken, L. Gai, Z. Shen, A. Rao, A. J. Musser, Tuning the coherent propagation of organic exciton-polaritons through dark state delocalization. *Adv. Sci.* **9**, e2105569 (2022).
79. D. Sannikov, T. Yagafarov, K. Georgiou, A. Zasedatelev, A. Baranikov, L. Gai, Z. Shen, D. Lidzey, P. Lagoudakis, Room temperature broadband polariton lasing from a dye-filled microcavity. *Adv. Opt. Mater.* **7**, 1900163 (2019).
80. L. Connolly, D. Lidzey, R. Butte, A. Adawi, D. Whittaker, M. Skolnick, R. Airey, Strong coupling in high-finesse organic semiconductor microcavities. *Adv. Opt. Mater.* **83**, 5377–5379 (2003).
81. T. Virgili, D. Coles, A. Adawi, C. Clark, P. Michetti, S. Rajendran, D. Brida, D. Polli, G. Cerullo, D. Lidzey, Ultrafast polariton relaxation dynamics in an organic semiconductor microcavity. *Phys. Rev. B* **83**, 245309 (2011).
82. K. E. McGhee, A. Putintsev, R. Jayaprakash, K. Georgiou, M. E. O'Kane, R. C. Kilbride, E. J. Cassella, M. Cavazzini, D. A. Sannikov, P. G. Lagoudakis, D. G. Lidzey, Polariton condensation in an organic microcavity utilising a hybrid metal-DBR mirror. *Sci. Rep.* **11**, 20879 (2021).
83. S. J. Byrnes, M. Khorasaninejad, F. Capasso, High-quality-factor planar optical cavities with laterally stopped, slowed, or reversed light. *Opt. Express* **24**, 18399–18407 (2016).
84. D. M. Coles, Q. Chen, L. C. Flatten, J. M. Smith, K. Müllen, A. Narita, D. G. Lidzey, Strong exciton–photon coupling in a nanographene filled microcavity. *Nano Lett.* **17**, 5521–5525 (2017).

Acknowledgments: We thank A. González-Tudela, E. Waks, X. Marie, and D. Wild for valuable discussions and enriching feedback on the manuscript. **Funding:** This work was supported by the NSF DMR-2145712, AFOSR FA9550-19-1-0399 and FA9550-22-1-0339, ONR N00014-20-1-2325, NSF IMOD DMR-2019444, ARL W911NF1920181, and Minta Martin and Simons Foundation. The sample fabrication was supported by the US Department of Energy, Office of Science, Office of Basic Energy Sciences Early Career Research Program under award no. DE-SC-0022885. K.W. and T.T. acknowledge support from the JSPS KAKENHI (grant numbers 20H00354, 21H05233, and 23H02052) and World Premier International Research Center Initiative (WPI), MEXT, Japan. This research used Quantum Material Press (QPress) of the Center for Functional Nanomaterials (CFN), which is a US Department of Energy Office of Science User Facility, at Brookhaven National Laboratory under contract no. DE-SC0012704. **Author contributions:** D.G.S.-F., S.S., M.J.M., R.N., Y.Z., and M.H. conceived and designed the experiments. S.S., D.G.S.-F., and M.J.M. performed the simulations. K.W., T.T., S.P., and H.J. supplied the necessary material for the fabrication of the sample. R.N. fabricated the samples. D.G.S.-F. and S.S. performed the experiments with assistance from E.M. and V.S. D.G.S.-F. and S.S. analyzed the data and interpreted the results with help from M.J.M. and A.G. D.G.S.-F. and S.S. wrote the manuscript, with input from all authors. All work was supervised by M.H. and Y.Z. **Competing interests:** The authors declare that they have no competing interests. **Data and materials availability:** All data needed to evaluate the conclusions in the paper are present in the figures of the paper and/or the Supplementary Materials. The data can also be accessed at https://doi.org/10.5281/zenodo.13737981.

Submitted 8 July 2024
Accepted 8 November 2024
Published 18 December 2024
10.1126/sciadv.adr5904